GEOPHYSICS, VOL. 61, NO. 1 (JANUARY-FEBRUARY 1996); P. 43–55, 12 FIGS., 2 TABLES.

Pressure in a fluid-filled borehole caused by a seismic source in stratified media

Chengbin Peng*, Jung M. Lee‡, and M. Nafi Toksöz‡

ABSTRACT

A method for numerically simulating hydrophone vertical seismic profiles (VSP) and crosswell data measured in a fluid-filled borehole (either open or cased) embedded in stratified media is presented. The method makes use of both the borehole coupling theory and the global matrix formulation for computing synthetic seismograms in a stratified medium. The global matrix formulation is used to calculate the stress field at the borehole location. Borehole coupling theory is then employed to obtain the pressure in the borehole fluid. Comparisons with exact solutions for an open borehole in a homogeneous and unbounded formation show that this method is accurate for frequencies below 2 kHz. This method is used to model the Kent Cliffs hydrophone VSP data, where good agreement between the numerical simulations and the field measurements has been found, in both traveltimes and rms amplitudes of the direct *P*-wave. Examples show that this method is efficient and accurate, and can be applied to model VSP and crosswell experiments using an array of hydrophones.

INTRODUCTION

Numerical simulation of elastic wave propagation in crosswell seismic profiling and vertical seismic profile (VSP) configurations has been extensively studied in recent years (Wyatt, 1981; Temme and Mueller, 1982; Sullivan, 1984; Suprajitno and Greenhalgh, 1986; Schmidt and Tango, 1986; Aminzadeh, 1989). These methods are suited to modeling only downhole geophone data at low frequencies, since the boreholes are not properly included. However, a variety of geophysical applications involve measuring the pressure inside a fluid-filled borehole for a source on the surface or in another borehole (Marzetta et al., 1988; Lee, 1990; Albright and Johnson, 1990; Krohn, 1992; Toksöz et al., 1992). Pressure measurement is advantageous because we use hydrophones, that are free from mechanical noises (e.g., poor clamping, tool resonance, asymmetric coupling), and are cost efficient compared to a downhole three-component clamped geophones (Marzetta et al., 1988). For hydrophone data modeling, the existing methods are not applicable because they are incapable of handling events associated with the borehole fluid and yield erroneous amplitudes for direct and reflected waves refracted at the fluid-solid interface. There is presently an increased demand for an efficient method of modeling hydrophone VSP and crosswell experiments (Kurkjian et al., 1994).

The objectives of this paper are to develop a useful method for computing the hydrophone response in VSP surveys and subsequently to model the field data from the Kent Cliffs hydrophone VSP experiment. Kurkjian et al. (1994) proposed a numerical technique for modeling downhole seismic data acquired with a hydrophone in crosswell configurations. In their method, the problem is divided into three parts: generation of the source well representation where the tube waves in the source well are taken into account, transmission from source well to receiver well using a preexisting code, and calculation of the hydrophone measurements by applying White's quasistatic approximation. The boreholes are discretized into small elements (10 points per tube wave wavelength). The size of the matrix equations is proportional to the number of discretization along the boreholes. The formulations given in their paper are valid for open boreholes. In contrast, in this work the borehole coupling process is incorporated into the global matrix algorithm for synthetic seismograms in a layered medium. No discretization along the borehole is required. The size of the matrix equations is proportional to the number of geological layers presented in the model. As a result, the formulations achieve both accuracy and computational speed. Our method is valid for open, cased, and partially filled boreholes. It agrees with analytical solutions

Presented at the 63rd Annual International Meeting, Society of Exploration Geophysicists. Manuscript received by the Editor December 30, 1993; revised manuscript received March 30, 1995.
*Formerly Earth Resources Laboratory, Dept. of Earth, Atmospheric, and Planetary Sciences, Massachusetts Institute of Technology, Cambridge, MA 02139; presently Geophysics Research Dept., Bellaire Research Center, Shell Development Company, P.O. Box 481, Houston, TX 77001-0481.
‡Earth Resources Laboratory, Dept. of Earth, Atmospheric, and Planetary Sciences, Massachusetts Institute of Technology, Cambridge, MA 02139.

in simplified media, and also predicts the traveltime and amplitude data of the Kent Cliffs hydrophone VSP experiment.

The first section of this paper presents a theoretical formulation for computing the pressure in a fluid-filled borehole for a seismic source in a stratified medium. Our method establishes an efficient tool for hydrophone data modeling at low frequencies. Its accuracy is validated by an analytical solution for the case where the formation is homogeneous. This is shown in the second section. The third section presents an application of our method to the Kent Cliffs borehole experiment. Using a stratified earth model derived from the averaged sonic well logging profiles, we find that this method predicts both the propagational (traveltime) and the dynamic characteristics (rms amplitude) of observed hydrophone data quite well. The last section summarizes the problem and gives a few conclusions.

THEORETICAL FORMULATION

Problem statement

The problem we consider is a vertical fluid-filled borehole in a horizontally layered half-space. As shown in Figure 1, each layer of the formation has a homogeneous visco-elastic medium with density ρ_m, compressional-wave speed α_m, and shear-wave speed β_m, in addition to the quality factors Q_{pm} and Q_{sm}, where m denotes the layer number with $1 \le m \le N + 1$. Here N is the total number of horizontal layers. The half-space $z_N < z < \infty$ is denoted as layer N + 1. The top surface of the mth layer is at depth z_{m-1} and the bottom surface is at depth z_m. The borehole is assumed to have a finite length and is filled with a fluid that has density ρ_f, compressional-wave speed α_f, and quality factor Q_f. Furthermore, the fluid fills only a portion of the borehole from the bottom at depth $z = H$ to the top at depth $z = z_0$ (water table), where $0 \le z_0 \le H$. The borehole can be either open, cased, or partially cased. In an open borehole, we use r_b to denote the radius of the borehole. In a cased borehole, there is a radial layer around the borehole with an inner radius r_b and an outer radius r_c. The casing is assumed to be homogeneous and elastic with compressional-wave speed α_c, shear-wave speed β_c, and density ρ_c. The top surface at $z = 0$ in the figure is assumed to be stress free. The goal is to compute the pressure disturbance produced in the fluid by the elastic wavefields radiated from a source in the formation.

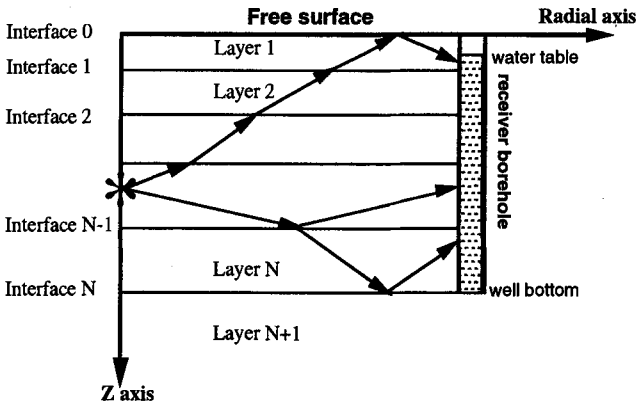

FIG. 1. A borehole in a stratified half-space. In each layer, the formation is homogeneous and viscoelastic. A seismic source is either on the free surface (VSP geometry) or inside the formation (crosswell geometry). An array of hydrophones is in the borehole. The borehole has a finite length and may be partially filled with fluid.

We are interested in the case where the borehole radius is much smaller than the wavelength in the formation, i.e., $r_b \ll \beta_{min}/f$, where β_{min} is the minimum shear velocity in the formation and f is the frequency. For a typical choice of parameters (r_b = 0.10 m, β_{min} = 2000 m/s), the frequency of an incident wave needs to be less than 2000 Hz for which the borehole radius is less than one-tenth of the shortest wavelength. This condition satisfies almost all VSP and crosswell experiments [for extreme cases, see Albright and Johnson (1990)].

Borehole coupling equation

At low frequencies, the pressure in the fluid is homogeneous across the borehole cross-section and is related to the deformation of an empty borehole by the following borehole coupling equation, written in the time domain as

$$\frac{\partial^2 P}{\partial z^2} - \frac{1}{C_T^2}\frac{\partial^2 P}{\partial t^2} = -2\rho_f \frac{\partial^2 \varepsilon_r}{\partial t^2}, \quad (1)$$

where $P(z, t)$ is the pressure in the fluid, C_T is the tube-wave velocity in an open or a cased borehole, and $\varepsilon_r(z, t) = \overline{[u_r(z, t)/r_b]}$ is the borehole squeeze strain associated with the incident waves. The overbar denotes an azimuthal average, and $u_r(z, t)$ is the radial displacement on the borehole wall. The derivation has been given in Peng (1993). In an open borehole, White (1953) gave

$$\varepsilon_r(z, \omega) = \frac{\sigma_{xx}(z, \omega) + \sigma_{yy}(z, \omega)}{E} - \nu\frac{\sigma_{zz}(z, \omega)}{E}, \quad (2)$$

where σ_{xx}, σ_{yy}, and σ_{zz} are the principal stresses of the incident waves around the vicinity of a borehole. E and ν are the Young's modulus and the Poisson's ratio of the formation, respectively. In a cased borehole, we obtain (Peng, 1993)

$$\varepsilon_r(z, \omega) = \frac{\sigma_{xx}(z, \omega) + \sigma_{yy}(z, \omega)}{E_\parallel} - \nu\frac{\sigma_{zz}(z, \omega)}{E_\perp}, \quad (3)$$

where $E_\parallel$ and $E_\perp$ are the effective moduli of the cased borehole against radial and vertical deformations, and are given by

$$E_\parallel = \frac{E}{1 + \zeta\nu}\left[1 + \left(\frac{\mu_c}{\mu} - 1\right)(1 - \gamma_c)\left(1 - \frac{r_b^2}{r_c^2}\right)\right],$$

and

$$E_\perp = \frac{E}{1 + \zeta\nu^{-1}}\left[1 + \left(\frac{\mu_c}{\mu} - 1\right)(1 - \gamma_c)\left(1 - \frac{r_b^2}{r_c^2}\right)\right],$$

where

$$\zeta = \left(\frac{\mu_c}{\mu} - 1\right)\left(\frac{1}{2} - \gamma_c\right)\left(1 - \frac{r_b^2}{r_c^2}\right),$$

and where $\gamma_c = \beta_c^2/\alpha_c^2$, μ and μ_c are the shear rigidities of the formation and casing, respectively. In the case where $r_b = r_c$ or $E_c = E$ and $\nu_c = \nu$, i.e., the casing vanishes, $E_\parallel$ and $E_\perp$ reduce

to E, the Young's modulus of the formation. Thus equation (3) reduces to equation (2). The derivations of equations (2) and (3) require that seismic wavelengths be much larger than the borehole radius. A rule of thumb would be that the shortest wavelength be at least ten times larger than the borehole radius, allowing accurate handling of S-waves.

Pressure in the fluid

Given that $\varepsilon_r(z, \omega)$, the borehole squeeze strain, is known, the pressure in the fluid can be obtained from equation (1). In a segment of the fluid column that is in the depth range of the mth layer of the formation, i.e., $z_{m-1} \le z \le z_m$ where z_{m-1} and z_m are the depths of the top and the bottom of the mth layer, respectively, the pressure is determined by

$$P(z, \omega) = A_m e^{-ik_m z} + B_m e^{ik_m z} + \rho_f \omega^2 \int_{z_{m-1}}^{z_m} \varepsilon_r^{(inc)}(z', \omega) \frac{i}{k_m} e^{-ik_m |z-z'|}\, dz', \quad (4)$$

where $k_m = \omega/C_T$ is the tube-wave wavenumber in the fluid associated with the mth layer, A_m and B_m are unknown coefficients representing the upgoing and downgoing energies in the fluid. The Green's function used in deriving this equation can be found in Morse and Feshbach (1953, 811).

The boundary conditions for determining A_m and B_m are the continuities of pressure and axial fluid velocity between layers m and $m + 1$, the vanishing of pressure at the top of the borehole fluid (water table), and the rigidity condition at the well bottom. These boundary conditions yield the following set of linear equations for the unknown coefficients:

$$\underline{\mathbf{D}}\mathbf{q} = \mathbf{c}, \quad (5)$$

where

$$\underline{\mathbf{D}} = \begin{pmatrix} e^{-ik_1 z_0}, & e^{ik_1 z_0}, & & & & \\ e^{-ik_m z_m}, & e^{ik_m z_m}, & -e^{-ik_{m+1} z_m}, & -e^{ik_{m+1} z_m}, & & \\ -ik_m e^{-ik_m z_m}, & ik_m e^{ik_m z_m}, & ik_{m+1} e^{-ik_{m+1} z_m}, & -ik_{m+1} e^{ik_{m+1} z_m}, & & \\ & & & & -ik_J e^{-ik_J H}, & ik_J e^{ik_J H} \end{pmatrix},$$

is a band matrix whose upper and lower bandwidths are equal to three, and

$$\mathbf{q} = [A_1, B_1, \ldots, A_m, B_m, A_{m+1}, B_{m+1}, \ldots, A_J, B_J]^T,$$

$$\mathbf{c} = \left[-w_1(z_0), \ldots, w_{m+1}(z_m) - w_m(z_m), \frac{dw_{m+1}(z_m)}{dz} - \frac{dw_m(z_m)}{dz}, \ldots, -\frac{dw_J(H)}{dz} \right]^T.$$

In the above equation, $w_m(z)$ denotes the third term on the right-hand side of equation (4), i.e.,

$$w_m(z) = \rho_f \omega^2 \int_{z_{m-1}}^{z_m} \varepsilon_r^{(inc)}(z', \omega) \frac{i}{k_m} e^{-ik_m |z-z'|}\, dz',$$

$$= i \frac{\rho_f \omega^2}{k_m} \left[\int_{z_{m-1}}^{z} \varepsilon_r^{(inc)}(z', \omega) e^{-ik_m (z-z')}\, dz' + \int_{z}^{z_m} \varepsilon_r^{(inc)}(z', \omega) e^{+ik_m (z-z')} dz' \right]. \quad (6)$$

Recall that z_0 is the depth of the water table and H is the depth of the well bottom. The subscript I is the index of the layer in which the water table is located (i.e., $z_{I-1} \le z_0 < z_I$), and J is the index of the layer where the well bottom is positioned (i.e., $z_{J-1} < H \le z_J$). It is assumed that $1 \le I \le m \le J \le N + 1$.

Borehole squeeze strain

In this section, we proceed to compute the pressure in the borehole fluid for a seismic source in a stratified formation. The pressure in the fluid can be obtained by solving matrix equation (5) if the borehole squeeze strain is known. To determine the borehole squeeze strain $\varepsilon_r(z, \omega)$ in equation (2) for an open borehole or in equation (3) for a cased borehole, we need to compute the stresses at the location of the presumed borehole. This is a much easier problem than the original one involving a fluid-filled borehole embedded in a layered half-space. For a stratified medium, the Thomson-Haskell type propagator matrix method can be used to achieve this goal (Harkrider, 1964; Takeuchi and Saito, 1972; Kennett and Kerry, 1979). We adopt an approach that combines the discrete wavenumber method (Bouchon, 1981) with the global matrix method (Chin et al., 1984, Schmidt and Tango, 1986) to efficiently and accurately compute the stress and displacement fields in a stratified half-space. The details of this approach are given in the Appendix.

In terms of the displacement-stress vector $\mathbf{B}(z; \omega, k, n) = [\tilde{U}, \tilde{V}, \tilde{P}, \tilde{S}]^T$ in equation (A-3) (see the Appendix), the borehole squeeze strain in equation (2) can be computed according to

$$\varepsilon_r(z, \omega) = \int_0^\infty \Gamma(z, \omega, k) J_0(kr_b) J_0(kr_0) k\, dk, \quad (7)$$

where

$$\Gamma(z, \omega, k) = \frac{\lambda}{2\mu(\lambda + 2\mu)} \tilde{P}(z; \omega, k, 0)$$

$$-\frac{2(\lambda+\mu)}{\lambda+2\mu}k\tilde{V}(z;\omega,k,0) \tag{8}$$

for an open borehole. For a cased borehole, it is

$$\Gamma(z,\omega,k)=\frac{\lambda}{2\mu(3\lambda+2\mu)}\left[\eta_{\parallel}\frac{4(\lambda+\mu)}{\lambda+2\mu}-\eta_{\perp}\right]\times\tilde{P}(z;\omega,k,0)-\eta_{\parallel}\frac{2(\lambda+\mu)}{\lambda+2\mu}k\tilde{V}(z;\omega,k,0). \tag{9}$$

In the above equation, ω is the frequency, k is the radial wavenumber, r_b is the borehole radius, r_0 is the horizontal distance between the seismic source and the fluid-filled borehole, and λ and μ are the Lamé's parameters. Here, $\eta_{\parallel}=E/E_{\parallel}$ and $\eta_{\perp}=E/E_{\perp}$ are the ratio of the effective Young's moduli in an open borehole to those in a cased borehole, and $J_0(x)$ is the Bessel function of the zeroth order. Substituting equation (7) into equation (6), after a few algebraic manipulations, we get

$$w_m(z,\omega)=i\frac{\rho_f\omega^2}{k_m}\int_0^{\infty}[\mathbf{k}_P^T(\mathbf{J}^+(z;\omega,k)+\mathbf{J}^-(z;\omega,k))-k\mathbf{k}_V^T(\mathbf{J}^+(z;\omega,k)+\mathbf{J}^-(z;\omega,k))]J_0(kr_b)J_0(kr_0)k\,dk, \tag{10}$$

where

$$\mathbf{k}_P=\frac{\lambda}{2\mu(3\lambda+2\mu)}\left[\eta_{\parallel}\frac{4(\lambda+\mu)}{\lambda+2\mu}-\eta_{\perp}\right][0,0,1,0]^T, \tag{11}$$

and

$$\mathbf{k}_V=\eta_{\parallel}\frac{2(\lambda+\mu)}{\lambda+2\mu}[0,1,0,0]^T \tag{12}$$

are two indication vectors that yield $\tilde{P}(z;\omega,k,n)$ and $\tilde{V}(z;\omega,k,n)$ from $\mathbf{B}(z;\omega,k,n)$, the displacement-stress vector in the frequency-horizontal wavenumber domain. In the above equation, $\mathbf{J}^+(z;\omega,k)$ and $\mathbf{J}^-(z;\omega,k)$ are vectors defined as

$$\mathbf{J}^+(z;\omega,k)=\int_{z_{m-1}}^{z}\mathbf{B}(z;\omega,k,n=0)e^{-ik_m(z-z')}\,dz', \tag{13}$$

and

$$\mathbf{J}^-(z;\omega,k)=\int_{z}^{z_m}\mathbf{B}(z;\omega,k,n=0)e^{+ik_m(z-z')}\,dz'. \tag{14}$$

The integration with respect to the horizontal wavenumber k is carried out first by the discrete wavenumber method (Bouchon and Aki, 1977; Bouchon, 1981). After $w_m(z,\omega)$ and $dw_m(z,\omega)/dz$ are computed, equations (5) and (4) are used to determine the pressure $P(z,\omega)$ in the fluid. Then an integration with respect to frequency is implemented by fast Fourier transform (FFT) to obtain the time response $P(z,t)$ at a given depth. The additional computation for borehole coupling is significantly less than the computation of the stress field around the borehole by the global matrix method. Therefore, this method is as fast as the existing ones that do not include the fluid-filled borehole. It is worthwhile to note that the borehole coupling equation can be incorporated into other numerical techniques that compute the normal stresses of incident waves, such as finite difference or dynamic ray-tracing methods. The global matrix algorithm is chosen because it provides general solutions that include inhomogeneous waves, and it can be incorporated efficiently as discussed above.

NUMERICAL EXAMPLES

To show the accuracy of this technique, we present a comparison with an analytical solution for a fluid-filled borehole in an unbounded and homogeneous formation. In this case, the pressure in the fluid can be computed exactly for an explosive source in the formation. The exact method is to express the wavefield caused by an explosive source as a superposition of plane waves. The coupling of individual plane waves into the borehole fluid is accomplished through the method described in Schoenberg (1986) and Peng et al. (1993). Finally, contributions from all of them are summed. In this example, the formation compressional velocity is 3000 m/s, shear velocity 2000 m/s, and density 2400 kg/m^3. The fluid in the borehole is ideal water. The borehole is uncased with a 0.10 m radius. The source is at depth η_s = 400 m with a horizontal offset r_0 = 400 m. A Kelly wavelet (Kelly et al., 1976) with a central frequency of 50 Hz is used as the source signal. We use 21 receivers that equally span a section of the borehole from depths of 0 to 800 m. Figure 2 shows two calculations: one is computed by the exact method, the other by the hybrid method developed in this paper. Up to the resolution in this figure, one cannot tell the difference between the calculations by our technique and those by the exact method. Then we take the Fourier transforms of both calculations and pick the spectral amplitudes at the central frequency of 50 Hz. After multiplying by the source receiver distance, i.e., the geometrical spreading correction, we plot the result shown in Figure 3 as a function of angle of incidence with respect to the borehole axis. This graphic representation of borehole data is also called the point-source reception pattern. In this figure, the open circle is from our numerical method, the solid circle corresponds to the exact solution, the solid triangle shows the pressure disturbance in a full space assuming the borehole is *absent*. The triangles, as expected, are on the unit circle for an explosive source. The circles are bent inward because of the pressure release on the fluid-solid interface at the borehole wall. Again the numerical data agree with the exact solutions in the frequency domain.

In the second example, we choose a configuration where a low velocity layer is embedded in a high velocity half-space. The depths of the top and bottom boundaries of the low velocity layer are at 300 m and 500 m, respectively. The borehole (radius r_b = 0.1 m) is open and filled with fluid (α_f = 1500 m/s, ρ_f = 1.0 g/cm^3 and Q_f = 30). It has a finite length of 800 m. The source is at depth 400 m and at offset 400 m. The receivers are in the borehole spanning a depth range between 0 to 800 m. The top surface is stress free. The source waveform is a Kelly wavelet with the central frequency of 100 Hz. The formation parameters for this calculation are given in Table 1. Figure 4 shows the synthetic seismograms of pressure in the borehole fluid. Clearly, a significant portion of energy is trapped in the low velocity layer (300–500 m depth interval),

arriving at a later time in the seismograms. Multiple reflections, occurring just after the first arrivals inside this layer, are observed. The low velocity events are tube waves generated at the interface boundaries as well as at the top and bottom of the borehole. The tube wave generated at the well head has a larger amplitude. Reflections at the free surface (top) are also discernible. On the free surface, the pressure is zero (first trace on the top).

The third example is a calculation for a cased borehole. The configuration and parameters are the same as the second example. The casing is steel with a 2 cm thickness. Figure 5 shows the synthetic pressure in the cased borehole. The amplitude of the fluid pressure is significantly reduced in a cased borehole. The maximum amplitude in Figure 4 is about three times larger than in Figure 5. The relative amplitudes of the trapped waves in the depth interval corresponding to the low velocity layer are not as prominent as those in an open borehole because the casing tends to smooth out the effect of formation discontinuities. In the cased borehole, the tube waves from the well head are more evident, as are the *P*- and *S*-waves outside the low velocity layer.

APPLICATIONS TO THE KENT CLIFFS HYDROPHONE VSP EXPERIMENT

Background

The Kent Cliffs borehole is an approximately 1-km deep test well located in southeastern New York. The borehole is drilled for the study of the crustal stress regime. Various geophysical and geological data were collected in this borehole, including core samples, well-logs, televiewer survey, hydraulic fracturing

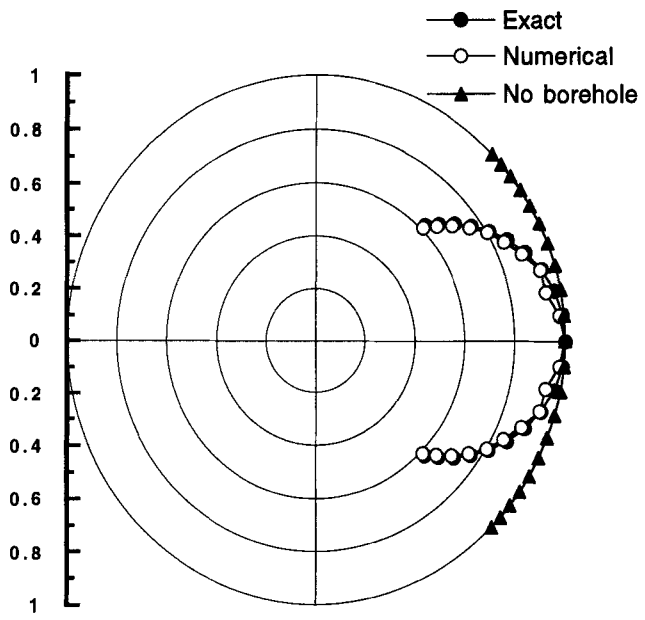

FIG. 3. Borehole point-source reception pattern for the example shown in Figure 2. The solid circles are data from the exact method. The open circles are data from the numerical method proposed in this chapter. The solid triangles are the isotropic radiation from an explosive source in a homogeneous and unbounded medium. The data are individually normalized. The reception pattern of a fluid-filled borehole shows a lobe at normal incidence.

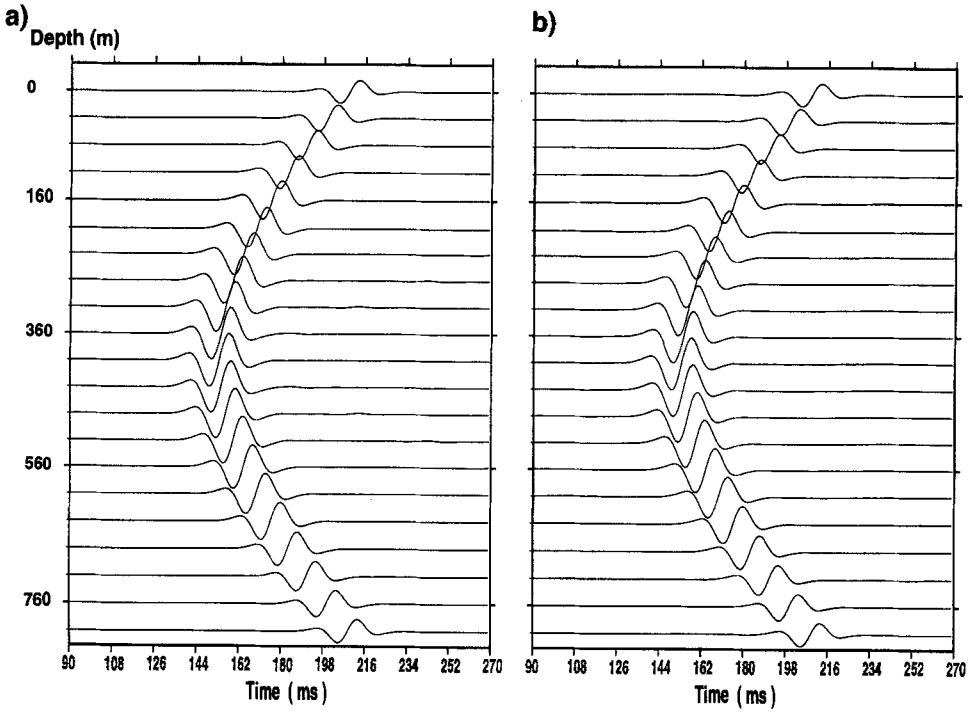

FIG. 2. Synthetic hydrophone pressures in the borehole fluid for an explosive source inside a homogeneous and unbounded formation: (a) by the numerical method developed in this paper, and (b) by an exact method. The parameters are: r_0 = 400 m, α = 3000 m/s, β = 2000 m/s, ρ = 2400 kg/m^3. The borehole radius is 0.10 m. The source waveform is a Kelly wavelet with a central frequency of 50 Hz. The depth of the source is 400 m. A total of 21 traces are plotted, spanning a depth range from 0 to 800 m.

stress measurements, and multiple offset VSPs with geophones and hydrophones. Geophysical and lithological data show that the borehole cuts first through fine-to-medium-grained amphibolite, the upper 10–40 m of the amphibolite is weathered, and the lower portion of the formation is gneiss. The transition zone is at a depth of 260–271 m in the borehole. The overall formation shows well developed foliation. The foliations and contact surfaces dip 60° southeast.

Core logs and downhole televiewer images show that there are two primary shear zones at depth intervals 273–275 m and 511–513 m. Fractures of various sizes are found at depths of 232, 286, and 512 m. Full waveform acoustic logs show that, in the overall depth interval of approximately 1 km, the compressional velocity varies between 5.8 km/s and 6.8 km/s and the shear velocity between 3.3 km/s and 3.6 km/s. The gradient of formation elastic properties with depth is small. For detailed accounts of this experiment, the reader is referred to Lee (1990) and Cicerone (1991). As a first-order approximation, we will ignore the dipping of the formation boundaries in our subsequent simulation.

Table 1. Medium parameters for the examples in Figure 4 and Figure 5.

Berea sandstone	depth (m)	P-velocity (m/s)	S-velocity (m/s)	density (g/cm^3)	Q_P	Q_S
Berea sandstone[1]	0–300	4206	2664	2.20	40	30
Shale sediment[2]	300–500	3000	1800	2.00	20	15
Berea sandstone	500–∞	4206	2664	2.20	40	30

[1]data from Toksöz, N. M., Johnston, D. H., and Timur, H. (1979).
[2]data from the experimental measurements at Chevron COFRC La Habra site.

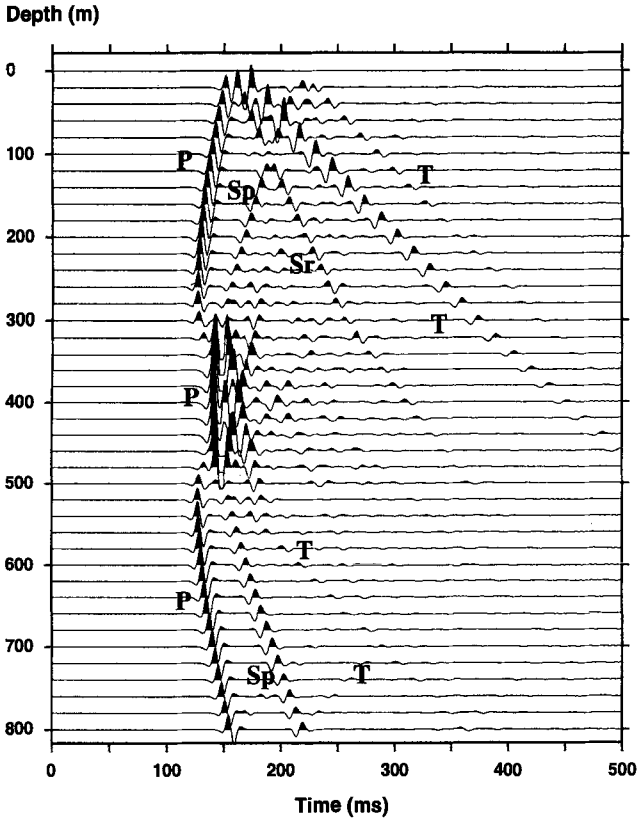

FIG. 4. Synthetic hydrophone pressures in an open borehole for an explosive source in the formation. The source is inside a low velocity layer embedded in a high velocity half-space. The source waveform is a Kelly wavelet with a central frequency of 100 Hz. The source-borehole offset is 400 m. The borehole radius is 0.10 m. Other parameters used in this calculation are given in Table 1. The maximum amplitude in this data set is 1.93E-02. The label P stands for P-wave, Sp for S-wave converted from P-wave, Sr for reflected S-wave, and T for tube wave.

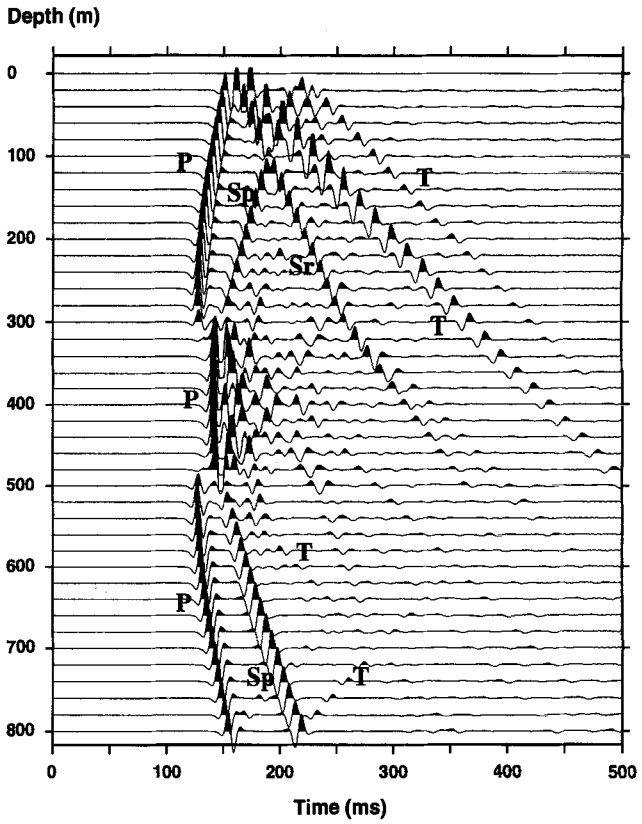

FIG. 5. Synthetic hydrophone pressures in a cased borehole for an explosive source in the formation. The source is inside a low velocity layer embedded in a high velocity half-space. The source waveform is a Kelly wavelet with a central frequency 100 Hz. The source-borehole offset is 400 m. The casing is steel. The inner radius of the casing is 0.10 m, the outer radius is 0.12 m. Other parameters used in this calculation are given in Table 1. The maximum amplitude in this data set is 6.37E-03. The label P stands for P-wave, Sp for S-wave converted from P-wave, Sr for reflected S-wave, and T for tube wave.

HYDROPHONE VSP DATA AND NUMERICAL MODELING

The multioffset hydrophone VSP experiment (Figure 6) was carried out using a repeatable vertical weight drop source on the surface. The receivers are an array of six (6) piezo-electric hydrophones separated by a 3.048-m interval. Four source offsets were used in the experiment. They are at 37.5, 350.5, 288.0, and 518.2 m away from the well head, and are referenced as S/P #1, S/P #2, S/P #3, and S/P #4, respectively, in the figure. Data processing includes raw data demultiplexing, stacking, and band-pass filtering. Figure 7 shows, as an example, the hydrophone VSP data at shot point S/P #3. A zero-phase band-pass filter with a pass band between 100–220 Hz is applied to these data. These data show large amplitude tube waves generated at the well head, the shear zones, and the fractures. The direct *P*- and *S*-waves are small in amplitude, and are strongly interfered with by the energetic tube waves. The tube waves originating from the well head are caused by the squeeze effect of incident *P*-, *S*-, and Rayleigh waves. The tube waves generated by shear zones and fractures are a result of the injection of fluid into the borehole as the incident *P*-wave and *S*-wave squeeze the fractures. The latter mechanism is extensively studied in the literature (Beydoun et al., 1985; Cicerone, 1991; Toksöz et al., 1992).

The modeling code developed in this paper does not have the ability to include fractures and shear zones in its formulation, thus we are unable to model the tube waves generated by them (i.e., the chevron-shaped patterns are absent in our synthetics). Nevertheless, other arrivals, such as *P*-, *S*-, and tube waves from the well head, are included.

We choose a stratified earth model described in Table 2. The formation *P*-wave and *S*-wave velocity profiles are derived from the sonic logging data. In Table 2, the lithology in each layer is also given. In the simulations, we use a vertical force on the surface to simulate the actual weight drop. The water table in the borehole is 14 m from the surface. The well bottom is approximately at 1007 m. Both of these numbers are from actual measurements. We use a Kelly wavelet with a central frequency of 100 Hz as the source signal. In the numerical simulation, the number of receivers is five times less than that of the field data. That is, we have 65 traces in the simulation instead of the 321 traces in the experiment. Nevertheless, the simulation covers approximately the same depth range as the experiment.

Figure 8 shows the synthetic hydrophone pressures for shot point S/P #3. In the synthetic seismograms, the *P*-, *S*-, and tube waves from the well head are well modeled. There are three tube wave events generated at the top of borehole (in both the field data and the numerical simulations as marked by the arrows): one is caused by the squeezing effect of the *P*-wave, another by the *S*-wave, and the last by the Rayleigh wave (ground roll). To quantitatively compare the numerical simulations with the field data, we pick the arrival time of the *P*-wave and measure its rms amplitude in a window of one period in length, that is,

$$P_{\text{rms}} = \sqrt{\frac{1}{T}\int_{t_0}^{t_0+T} p(t) \times p(t)\, dt},$$

where t_0 is the *P*-wave arrival time, T is the period equal to the reciprocal of the central frequency, and $p(t)$ is the hydrophone pressure data. The rms amplitude is also a measure of the energy in the time window. We plot both t_0 and P_{rms} as

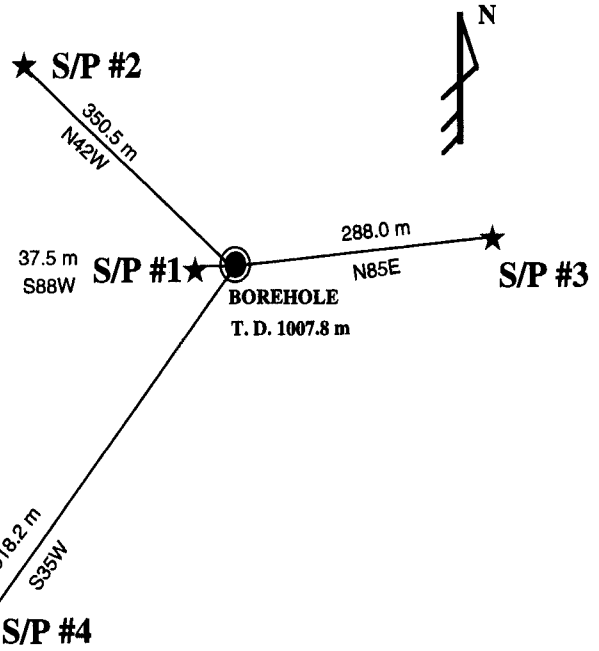

FIG. 6. A map showing the Kent Cliffs hydrophone VSP experiment. A total of four (4) shot points around the borehole were used in the experiment. The borehole has a depth about 1 km and is slightly deviated southeast by about 30 m in the east direction and 70 m in the south direction. The formation is amphibolite and gneiss in the top and bottom portions of the borehole, respectively, and is tilted toward the southeast by as much as 60°.

Table 2. Medium parameters and lithologies derived from logging data in the Kent Cliffs test borehole: The intrinsic attenuation is ignored in the synthetic calculation.

Lithology	depth (m)	*P*-velocity (m/s)	*S*-velocity (m/s)	density (g/cm^3)	Q_P	Q_S
Amphibolite	0–10	5500	3300	2.80	∞	∞
Amphibolite	10–85	6246	3700	2.90		
Amphibolite	85–215	6888	3850	3.10		
Transition zone	215–270	6189	3590	3.00		
Gneiss	270–425	6197	3530	2.90		
Gneiss	425–470	6197	3500	2.80		
Gneiss	470–770	6197	3530	2.90		
Gneiss	770–∞	6204	3630	2.90		

functions of hydrophone depth. The results are shown in Figure 9 through Figure 12.

Figure 9a shows the *P*-wave traveltime versus hydrophone depth for shot point S/P #1 (37.5 m horizontal offset). The solid line is the traveltime measured from the field data; the + symbol is that from the synthetics. The agreement is excellent, showing that the velocity model based on information from the sonic well logging data explains the traveltime of the VSP data at near offsets. In Figures 9b and 9c, we show the *P*-wave traveltime for shot points S/P #2 (350 m horizontal offset) and S/P #3 (288 m horizontal offset). At these shot points, the traveltimes in the synthetics are slightly different from those in the field data, which is attributed to the fact that the formation is actually tilted towards the southeast. Since the seismic velocity of the upper amphibolite layer is higher than that of the lower gneiss layer, the synthetic *P*-wave traveltimes are smaller than the observed ones in S/P #2, the northwest offset, while opposite phenomena occur in S/P #3, the east offset.

More importantly, our simulation can predict the dynamic behavior of a downhole hydrophone measurement as well. In Figure 10, we plot the *P*-wave rms amplitude versus depth for shot point S/P #1. In this plot, the solid line is the rms amplitude of the synthetic data; the + symbol is that of the field data. The integrated rms amplitude in the depth interval

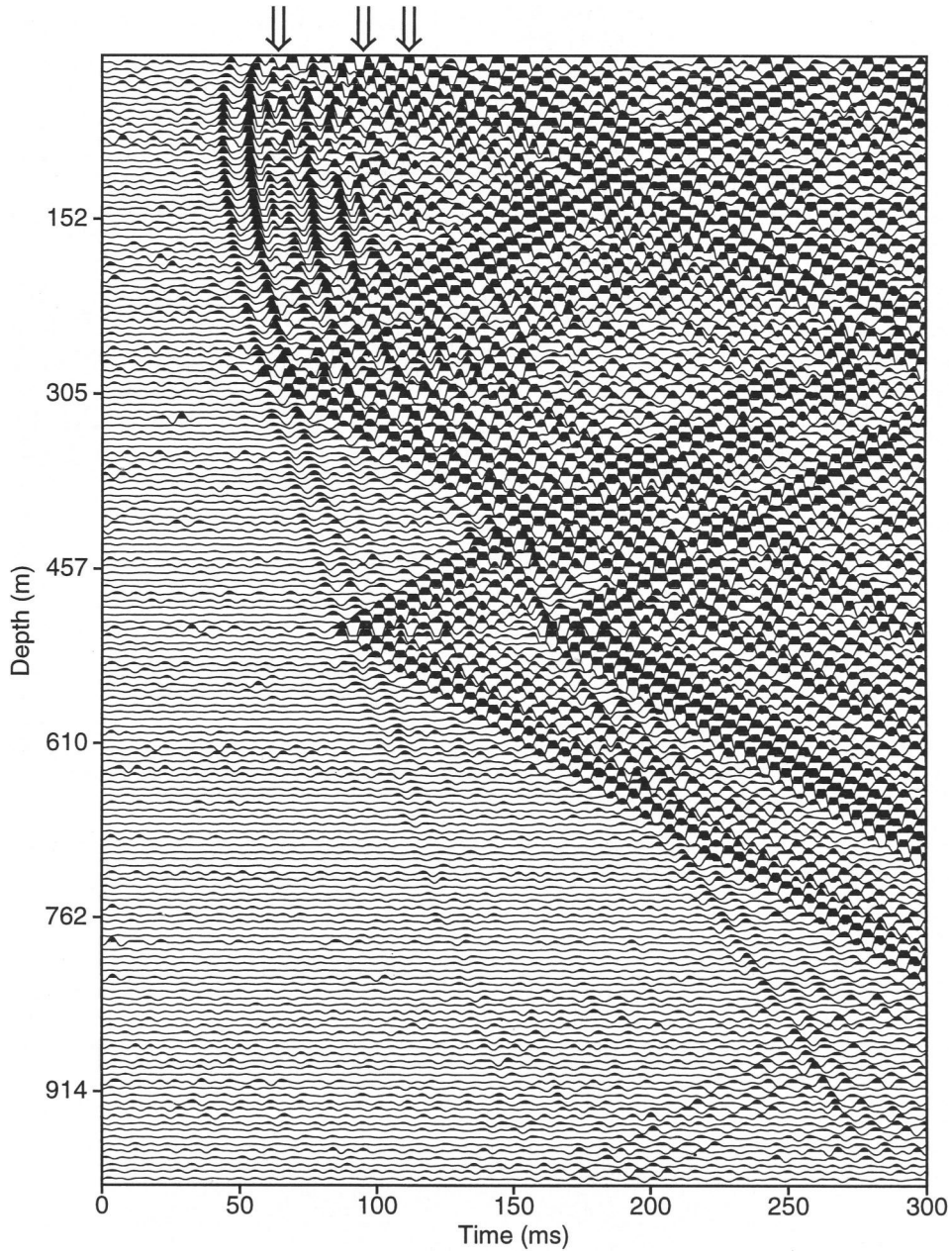

FIG. 7. Hydrophone VSP data for shot point S/P #3. The source offset is 288.0 m in the direction N85°E. The first hydrophone is at a depth of 15.25 m, slightly below the water table. The last hydrophone is at 990.6 m, slightly above the well bottom. A band-pass filter is applied to this data with a pass band between 100 Hz and 220 Hz.

304.8–990.6 m is used to scale the synthetic and the field data. There is a good agreement between the synthetic amplitude and the observed one, except at locations where tube waves are generated and interfere with the *P*-wave. This kind of agreement also exists for the other two shot points—S/P #2 and S/P #3—as shown in Figure 11 and Figure 12. For shot points at large offsets, however, the observed data points tend to shift away from the synthetic prediction at shallow depths, which is partly because of the assumption made in building the velocity model for synthetic computations. Note that complicated inhomogeneities around the surface were not included in the modeling either. At small offsets, the first-arrival *P*-wave energy decreases with receiver depth at a faster rate than an exponential; while at large offsets, exponential decays are observed. This ability of accurately predicting the amplitude of field data can be important for downhole seismic data interpretation and inversion for subsurface physical parameters.

DISCUSSIONS AND CONCLUSIONS

In this paper, an efficient and accurate method is proposed to model hydrophone VSP and crosswell data in a stratified

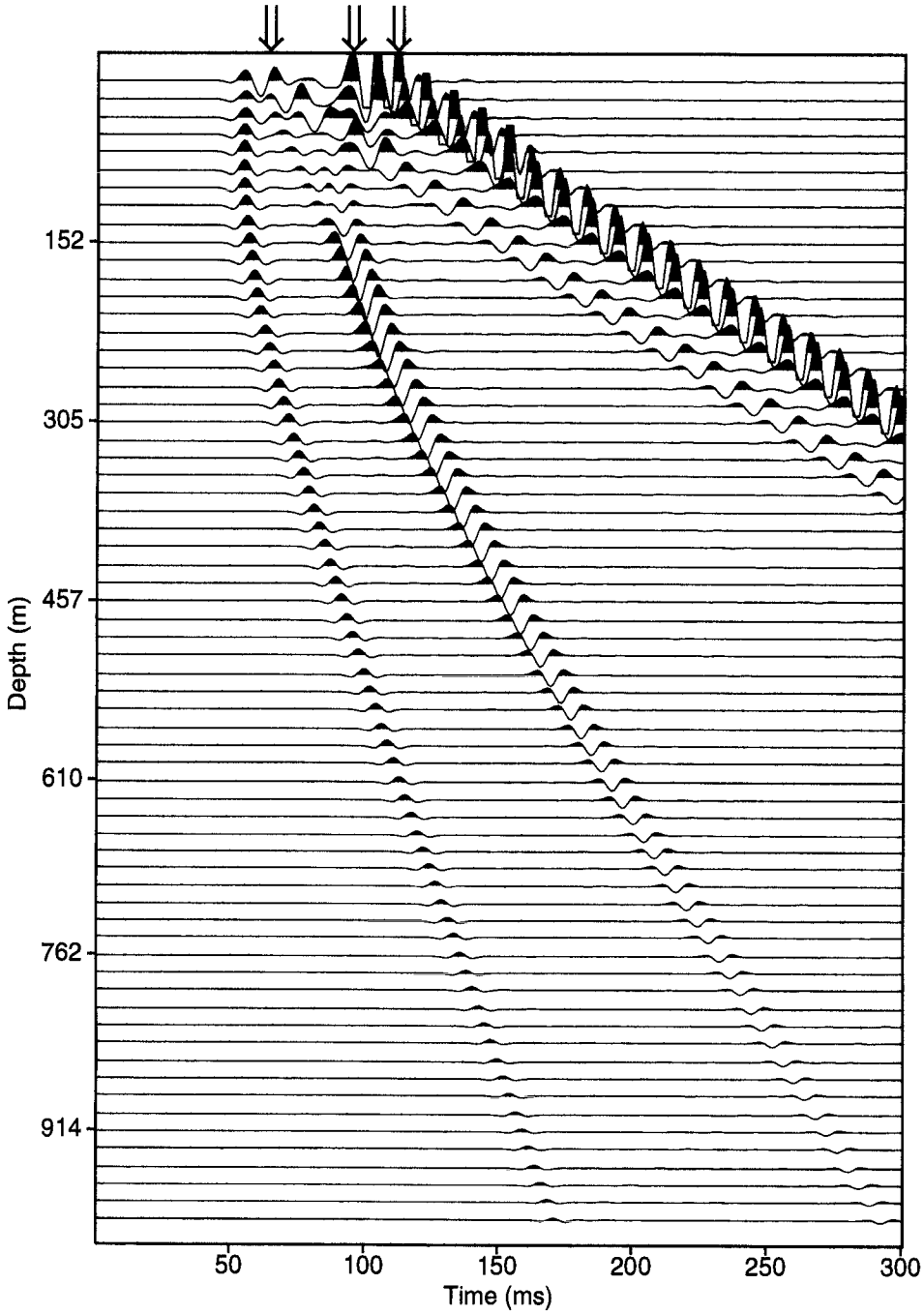

FIG. 8. Synthetic hydrophone VSP data for shot point S/P #3, computed with a stratified model for the formation. The source is a vertical force near the free surface, simulating the actual weight drop. The source waveform is a Kelly wavelet with a central frequency of 100 Hz. Others parameters are given in Table 2.

formation. This method incorporates borehole coupling theory into the global matrix algorithm by dividing the problem into two parts: propagation from the source to the presumed borehole location by the global matrix algorithm, and coupling the resulting stresses into the borehole fluid by a low-frequency approximation. This approach greatly reduces the difficulties of the original problem; viz., the inclusion of a fluid-filled borehole in a stratified medium that involves two sets of interfaces perpendicular to each other. It yields accurate results at frequencies below 2 kHz (for typical sedimentary rocks). This is demonstrated by a comparison with an analytical solution. The method is as fast as other existing ones in modeling elastic wave propagation in a layered medium.

This method has been applied to model the Kent Cliffs hydrophone VSP data. Using a stratified model derived from the sonic logging data, we are able to predict the traveltime

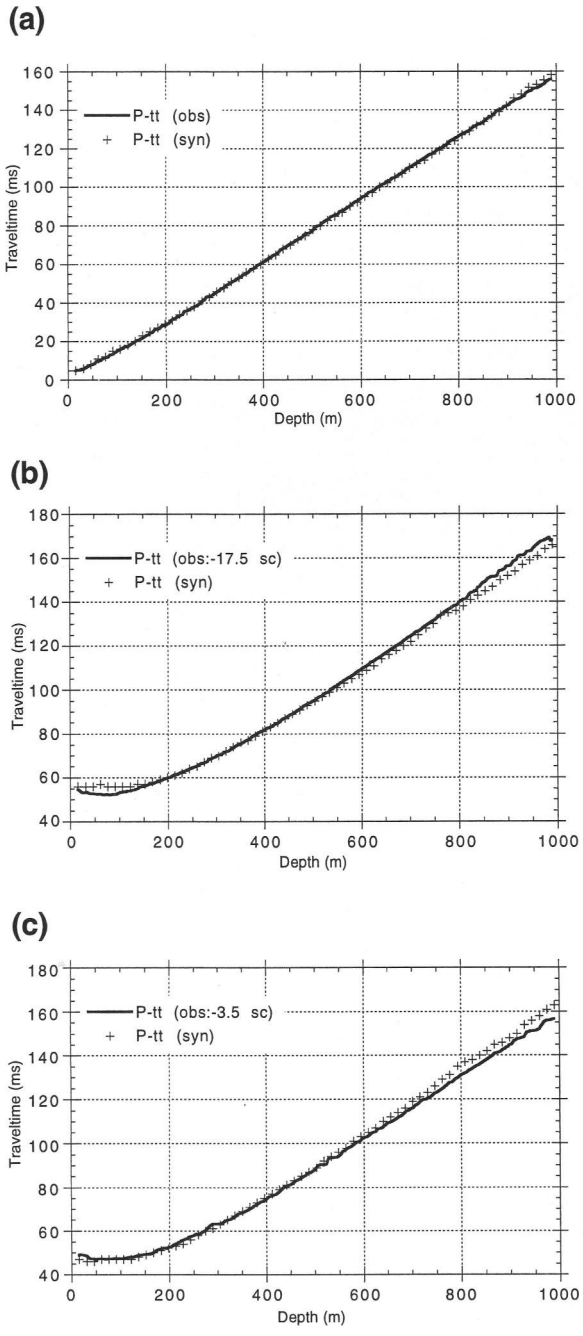

FIG. 9. *P*-wave traveltimes for shot points S/P #1 (a), S/P #2 (b), and S/P #3 (c). The solid line is the traveltime picked from the field hydrophone measurements shown in Figure 7. The plus (+) symbol is the traveltime picked from the synthetic hydrophone pressure shown in Figure 8. The horizontal axis is the depth of receivers in m. The vertical axis is traveltime in ms.

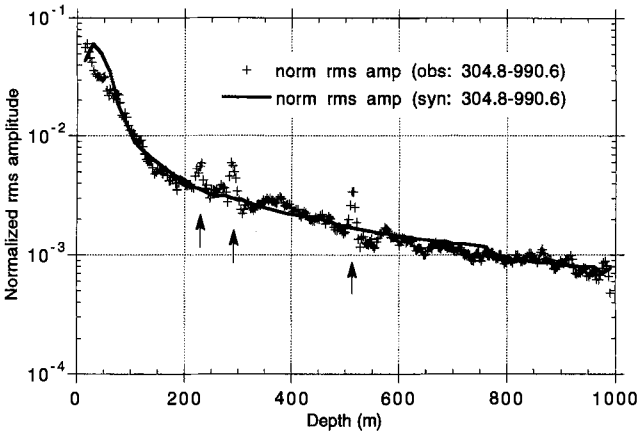

FIG. 10. The rms amplitudes of the first arrival (*P*-wave) for shot point S/P #1. The solid line is the rms amplitude computed from the synthetic hydrophone pressure. The plus (+) symbol is the rms amplitude derived from the field hydrophone measurement. A constant factor derived from data in the depth range between 304.8 m and 990.6 m is used to normalize the synthetic and field data. The horizontal axis is the depth of receivers in m. The vertical axis is the normalized rms amplitude in a logarithmic scale. The arrows indicate locations where tube waves generated by fractures interfere with the *P*-wave signals.

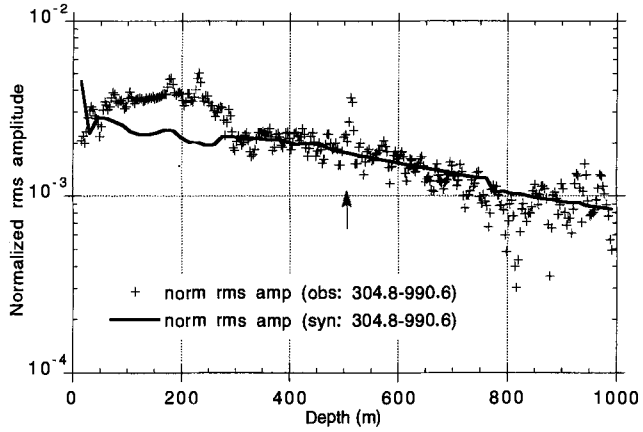

FIG. 11. The rms amplitude of the first arrival (*P*-wave) for shot point S/P #2. The solid line is the rms amplitude computed from the synthetic hydrophone pressure. The plus (+) symbol is the rms amplitude derived from the field hydrophone measurement. A constant factor derived from data in the depth range between 304.8 m and 990.6 m is used to normalize the synthetic and field data. The horizontal axis is the depth of receivers in m. The vertical axis is the normalized rms amplitude in a logarithmic scale. The arrow indicates the location where tube waves generated by fractures interfere with the *P*-wave signals.

and rms amplitude of the *P*-wave arrival in the hydrophone data, especially for the first shot point S/P #1. Our simulation demonstrates that the earth model based on the sonic well logging data explains the hydrophone VSP data at small offsets. There are systematic discrepancies between predictions and observations in the other two shot points (S/P #2 and S/P #3). These differences are attributed to the dipping of the formation (geological data show that the layers are tilted toward the southeast with a dip angle of 60°), incomplete knowledge of the structures and lithologies away from the borehole, and surface complications such as topography and weathered rocks.

Besides applications to hydrophone VSP data simulation, this method can be used to model crosswell data (including crosswell continuity logging) if proper source borehole effects are taken into account (Ben-Menahem and Kostek, 1991; Kurkjian et al., 1994; Gibson, 1992; Gibson and Peng, 1994). One limitation of this method would be the transmission of high-frequency signals over large distances, because the computation time increases linearly with both frequency and the maximum distance between the source and the receivers. However, this computational problem can be minimized by using fast computers.

ACKNOWLEDGMENTS

This work is supported in part by the Department of Energy (Grant No. DE-FG02-86ER13636) and also in part by the Reservoir Delineation Consortium and the nCUBE/ERL Geophysical Center for Parallel Processing at the Earth Resources Laboratory, Massachusetts Institute of Technology. All computations in this paper are performed on the nCUBE-2 parallel computer. We thank Dr. E. E. Charrette for helping us with the parallel programming.

REFERENCES

Aki, K., and Richards, P. G., 1980, Quantitative seismology: Theory and methods: W. H. Freeman & Co.

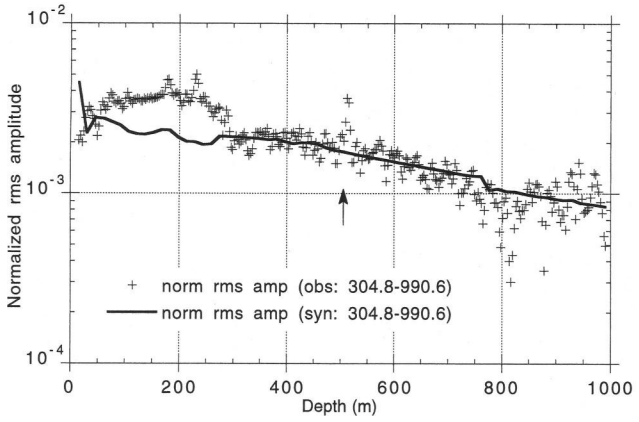

FIG. 12. The rms amplitude of the first arrival (*P*-wave) for shot point S/P #3. The solid line is the rms amplitude computed using the synthetic hydrophone pressure shown in Figure 7. The plus (+) symbol is the rms amplitude derived from the field hydrophone measurement shown in Figure 8. A constant factor derived from data in the depth range between 304.8 m and 990.6 m is used to normalize the synthetic and field data. The horizontal axis is the depth of receivers in m. The vertical axis is the normalized rms amplitude in a logarithmic scale. The arrows indicate locations where tube waves generated by fractures interfere with the *P*-wave signals.

Albright, J. N., and Johnson, P. A., 1990, Cross-borehole observation of mode conversion from borehole Stoneley waves to channel waves at a coal layer: Geophys. Prosp., **38**, 607–620.
Aminzadeh, F., 1989, Applications of elastic modeling in processing and interpretation of VSP data: a case study: Geophys. Prosp., **37**, 893–906.
Ben-Menahem, A., and Kostek, S., 1991, The equivalent force system of a monopole source in a fluid-filled open borehole: Geophysics, **56**, 1477–1481.
Ben-Menahem, A., and Singh, S. J., 1981, Seismic waves and sources: Springer-Verlag.
Beydoun, W. B., Cheng, C. H., and Toksöz, M. N., 1985, Detection of open fractures with vertical seismic profiling: J. Geophys. Res., **90**, 4557–4566.
Bouchon, M., 1981, A simple method to calculate Green's function for elastic layered media: Bull. Seis. Soc. Am., **71**, 959–971.
Bouchon, M., and Aki, K., 1977, Discrete wavenumber representation of seismic-source wave fields: Bull. Seis. Soc. Am., **67**, 259–277.
Cicerone, R. D., 1991, Detection and characterization of in-situ fractures in the Earth from vertical seismic profiling data: Ph.D. thesis, Massachusetts Inst. Tech.
Chin, R. C. Y., Hedstrom, G. W., and Thigpen, L., 1984, Matrix methods in synthetic seismograms: Geophys. J. Roy. Astr. Soc., **77**, 483–502.
Gibson, R. L., 1992, Models of seismic wave radiation from borehole sources in fast and slow formations: 62th Ann. Internat. Mtg., Soc. Expl. Geophys., Extended abstracts, 133–136.
Gibson, R. L., and Peng, C., 1994, Low- and high-frequency radiation from seismic sources in cased boreholes: Geophysics, **59**, 1780–1785.
Harkrider, D. G., 1964, Surface waves in multilayered elastic media: I. Rayleigh and Love waves from buried sources in a multilayered elastic half-space: Bull. Seis. Soc. Am., **54**, 627–679.
Kelly, K. R., Ward, R. W., Treitel, S., and Alford, R. M., 1976, Synthetic seismograms: A finite-difference approach: Geophysics, **41**, 2–27.
Kennett, B. L. N., and Kerry, N. J., 1979, Seismic waves in a stratified half-space: Geophys. J. Roy. Astr. Soc., **57**, 557–583.
Krohn, C. E., 1992, Crosswell continuity logging using guided seismic waves: The Leading Edge, **11**, no. 7, 39–45.
Kurkjian, A. L., Coates, R. T., White, J. E., and Schmidt, H., 1994, Finite-difference and frequency-wavenumber modeling of seismic monopole sources and receivers in fluid-filled boreholes: Geophysics, **59**, 1053–1064.
Lee, J. M., 1990, In-situ seismic anisotropy and its relationship to crack and rock fabrics: Ph.D. thesis, Pennsylvania State Univ.
Marzetta, T. L., Orton, M., Krampe, A., Johnston, L. K., and Wuenschel, P. C., 1988, A hydrophone vertical seismic profiling experiment: Geophysics, **53**, 1437–1444.
Morse, P., and Feshbach, H., 1953, Methods of theoretical physics: McGraw-Hill Book Co.
Peng, C., 1993, Borehole effects on downhole seismic measurements: Ph.D. thesis, Massachusetts Inst. Tech.
Peng, C., Cheng, C. H., and Toksöz, M. N., 1993, Borehole effect on downhole seismic measurements: Geophys. Prosp., **41**, 883–912.
Schmidt, H., and Tango, G., 1986, Efficient global matrix approach to the computation of synthetic seismograms: Geophys. J. Roy. Astr. Soc., **84**, 331–359.
Schoenberg, M., 1986, Fluid and solid motion on the neighborhood of a fluid-filled borehole due to the passage of a low frequency elastic plane wave: Geophysics, **51**, 1191–1205.
Sullivan, M. F., 1984, Finite element modeling of VSP data, *in* Toksöz, M. N., and Stewart, R. R., Eds., Vertical seismic profiling: Handbook of geophys. expl., **14B**, Geophys. Press, 45–62.
Suprajitno, M., and Greenhalgh, S. S., 1986, Theoretical vertical seismic profiling seismograms: Geophysics, **51**, 1252–1265.
Takeuchi, H., and Saito, H., 1972, Seismic surface waves, *in* Bolt, B. A., Ed., Method of Computational Physics, **11**: Academic Press, 217–295.
Temme, P., and Muller, G., 1982, Numerical simulation of vertical seismic profiling: J. Geophys., **50**, 177–188.
Toksöz, M. N., Cheng, C. H., and Cicerone, R. D., 1992, Fracture detection and characterization from hydrophone vertical seismic profiling data, *in* Evans, B. and Wong, T., Eds., Fault mechanics and transport properties of rocks: Academic Press, 389–414.
Toksöz, N. M., Johnston, D. H., and Timur, H., 1979, Attenuation of seismic waves in dry and saturated rocks: I. Laboratory measurements: Geophysics, **44**, 681–690.
White, J. E., 1953, Signals in a borehole due to plane waves in the solid: J. Acoust. Soc. Am., **25**, 906–915.
Van Schaack, M., Harris, J. M., Rector, J. W., and Lazaratos, S. K., 1992, High resolution cross-well imaging of a west Texas carbonate reservoir: Part 2. Wavefield analysis and tomography: 62th Ann. Internat. Mtg., Soc. Expl. Geophys., Expanded Abstracts, 40–44.
Wyatt, K. D., 1981, Synthetic vertical seismic profiles: Geophysics, **46**, 880–891.

APPENDIX A
THE GLOBAL MATRIX METHOD

Consider a vertically stratified half-space with a source or a vertical array of sources located on the coordinate axis (see Figure 1 without the borehole). In terms of the surface vector harmonics in the cylindrical coordinate system (R, θ, z), the displacement $\mathbf{u}$ and traction $\mathbf{t}$ across a surface perpendicular to the z-axis can be expressed as (Takeuchi and Saito, 1972; Chin et al., 1984)

$$\mathbf{u}(R, \theta, z) = \frac{1}{2\pi}\int_{-\infty}^{\infty} d\omega\, e^{i\omega t}\int_0^{\infty} k\, dk \times \sum_{n=-\infty}^{\infty} (\tilde{U}\mathbf{R}_k^n + \tilde{V}\mathbf{S}_k^n + \tilde{W}\mathbf{T}_k^n), \quad \text{(A-1)}$$

and

$$\mathbf{t}(R, \theta, z) = \frac{1}{2\pi}\int_{-\infty}^{\infty} d\omega\, e^{i\omega t}\int_0^{\infty} k\, dk \times \sum_{n=-\infty}^{\infty} (\tilde{P}\mathbf{R}_k^n + \tilde{S}\mathbf{S}_k^n + \tilde{T}\mathbf{T}_k^n), \quad \text{(A-2)}$$

where $\mathbf{R}_k^n$, $\mathbf{S}_k^n$, and $\mathbf{T}_k^n$ are vector harmonics in a cylindrical coordinate. The coefficients $\tilde{U}$, $\tilde{V}$, $\tilde{W}$, $\tilde{P}$, $\tilde{S}$ and $\tilde{T}$ are functions of depth z, frequency ω, horizontal wavenumber k, and order of harmonics n. They are related to each other by a first-order matrix equation

$$\frac{\partial}{\partial z}\mathbf{B} = \underline{A}(z; \omega, k)\mathbf{B}, \quad \text{(A-3)}$$

where $\mathbf{B}(z; \omega, k, n) = [\tilde{U}, \tilde{V}, \tilde{P}, \tilde{S}]^T$ is the displacement-stress vector for a *P-SV* problem and $\mathbf{B}(z; \omega, k, n) = [\tilde{W}, \tilde{T}]^T$ for a *SH* problem. In this paper, we focus our attention to the *P-SV* problem only. In this case

$$\underline{A}(z; \omega, k) = \begin{bmatrix} 0 & k(1-2\gamma) & 1/(\lambda+2\mu) & 0 \\ -k & 0 & 0 & 1/\mu \\ -\rho\omega^2 & 0 & 0 & k \\ 0 & -\rho\omega^2 + 4k^2\mu(1-\gamma) & -k((1-2\gamma) & 0 \end{bmatrix},$$

where $\gamma = \mu/(\lambda + 2\mu) = \beta^2/\alpha^2$, λ and μ are the Lamé parameters and ρ is the density. They are dependent on z.

For the case where the formation is layered, the elements of matrix $\underline{A}$ are piecewise constant such that the resulting equation has constant coefficients in each subinterval. In forming a global matrix solution to equation (A-3), the continuity of the local solution at an interface is required, i.e.,

$$\mathbf{B}_m(z_m^-; \omega, k, n) = \mathbf{B}_{m+1}(z_m^+; \omega, k, n), \quad m = 1, 2, \ldots, N.$$

In addition, the free surface condition at $z = 0$ and the radiation condition at $z \to \infty$ must be satisfied. The source is introduced as an equivalent discontinuity in the stress-displacement field across the source plane $z = \eta_s$ (Kennett and Kerry, 1979, Chin et al., 1984):

$$\mathbf{B}(\eta_s^+; \omega, k, n) - \mathbf{B}(\eta_s^-; \omega, k, n) = \mathbf{S}^*(\omega, k, n),$$

where, for a point volume source $\mathbf{S}^* = [-2, 0, 0, -4\mu k]^T$ (Harkrider, 1964); and for a vertical point force $\mathbf{S}^* = [0, 0, -1/2\pi, 0]^T$ (Harkrider, 1964; Bouchon, 1981). Other types of sources are constructed from the fundamental ones, and can be found in, among others, Ben-Menahem and Singh (1981).

Using the spectral decomposition of $\underline{A}_m = \underline{D}_m\underline{\Lambda}_m\underline{D}_m^{-1}$, we can rewrite equation (A-3) as

$$\frac{d}{dz}\mathbf{Q}_m = \underline{\Lambda}_m\mathbf{Q}_m, \quad z_{m-1} < z < z_m, \quad m = 1, 2, \ldots, N \quad \text{(A-4)}$$

where $\mathbf{Q}_m = \underline{D}_m^{-1}\mathbf{B}_m$. In the *P-SV* problem the choice of

$$\underline{D}_m = \begin{bmatrix} \nu_{\alpha m} & k & \nu_{\alpha m} & k \\ -k & -\nu_{\beta m} & k & \nu_{\beta m} \\ -\mu_m(2k^2 - k_{\beta m}^2) & -2\mu_m k\nu_{\beta m} & \mu_m(2k^2 - k_{\beta m}^2) & 2\mu_m k\nu_{\beta m} \\ 2\mu_m k\nu_{\alpha m} & \mu_m(2k^2 - k_{\beta m}^2) & 2\mu_m k\nu_{\alpha m} & \mu_m(2k^2 - k_{\beta m}^2) \end{bmatrix}$$

leads to

$$\underline{\Lambda}_m = \begin{bmatrix} -\nu_{\alpha m} & & & \\ & -\nu_{\beta m} & & \\ & & \nu_{\alpha m} & \\ & & & \nu_{\beta m} \end{bmatrix},$$

where $\nu_{\alpha m} = \sqrt{k^2 - k_{\alpha m}^2}$, $\nu_{\beta m} = \sqrt{k^2 - k_{\beta m}^2}$, $k_{\alpha m} = \omega/\alpha_m$, $k_{\beta m} = \omega/\beta_m$. α_m and β_m are the compressional and shear velocities in the layer m. Anelastic attenuation is incorporated into the formulation by making the medium velocities complex numbers (Aki and Richards, 1980). The choice of branch cuts is $\mathbf{R}(\nu_{\alpha m}) \geq 0$ and $\mathbf{R}(\nu_{\beta m}) \geq 0$ (i.e., the real part should not be less than zero) for the particular choice of $e^{i\omega t}$ time dependence.

The solution to equation (A-4) can be written in terms of a propagator matrix

$$\mathbf{Q}_m(z) = \exp[\underline{\Lambda}_m(z - z_{m-1})]\mathbf{Q}_m(z_{m-1}^+), \quad z_{m-1} < z < z_m, \quad m = 1, 2, \ldots, N \quad \text{(A-5)}$$

which relates the wavefield at the boundary to that in the interior. Knowing the vector $\mathbf{Q}_m(z)$ at the boundaries, the displacement-stress vector $\mathbf{B}_m$ can be readily computed by

$$\mathbf{B}_m(z; \omega, k, n) = \underline{D}_m \exp[\underline{\Lambda}_m(z - z_{m-1})]\mathbf{Q}_m(z_{m-1}^+). \quad \text{(A-6)}$$

To determine $\mathbf{Q}_m(z_{m-1}^+)$, the upgoing and downgoing amplitudes at the top boundary of the mth layer, the continuities

of stress and displacements across the interfaces are imposed, in addition to vanishing stresses at the free surface and the radiation condition at infinity. Let us denote

$$\underline{\mathbf{D}}_m = \begin{bmatrix} \underline{\mathbf{M}}_m^- & \underline{\mathbf{M}}_m^+ \\ \underline{\mathbf{N}}_m^- & \underline{\mathbf{N}}_m^+ \end{bmatrix},$$

$$\exp\left[\underline{\Lambda}_m(z_m - z_{m-1})\right] = \begin{bmatrix} \underline{\mathbf{E}}_m & \\ & \underline{\mathbf{E}}_m^{-1} \end{bmatrix},$$

where

$$\underline{\mathbf{E}}_m = \begin{bmatrix} \exp\left(-\nu_{\alpha m}(z_m - z_{m-1})\right) & 0 \\ 0 & \exp\left(-\nu_{\beta m}(z_m - z_{m-1})\right) \end{bmatrix}.$$

Also denote

$$\mathbf{Q}_m = \begin{bmatrix} \mathbf{p}_m^- \\ \mathbf{p}_m^+ \end{bmatrix},$$

where $\mathbf{p}_m^-$ corresponds to the downgoing amplitude and $\mathbf{p}_m^+$ corresponds to the upgoing amplitude in the mth layer. Then the interface boundary conditions can be written as

$$\begin{bmatrix} \underline{\mathbf{M}}_{m+1}^- & \underline{\mathbf{M}}_{m+1}^+ \\ \underline{\mathbf{N}}_{m+1}^- & \underline{\mathbf{N}}_{m+1}^+ \end{bmatrix} \begin{bmatrix} \mathbf{p}_{m+1}^- \\ \mathbf{p}_{m+1}^+ \end{bmatrix} - \begin{bmatrix} \underline{\mathbf{M}}_m^- & \underline{\mathbf{M}}_m^+ \\ \underline{\mathbf{N}}_m^- & \underline{\mathbf{N}}_m^+ \end{bmatrix} \begin{bmatrix} \underline{\mathbf{E}}_m & \\ & \underline{\mathbf{E}}_m^{-1} \end{bmatrix} \begin{bmatrix} \mathbf{p}_m^- \\ \mathbf{p}_m^+ \end{bmatrix} = \mathbf{0}, \quad \text{(A-7)}$$

except the source layer $m = s$ at which

$$\begin{bmatrix} \underline{\mathbf{M}}_{s+1}^- & \underline{\mathbf{M}}_{s+1}^+ \\ \underline{\mathbf{N}}_{s+1}^- & \underline{\mathbf{N}}_{s+1}^+ \end{bmatrix} \begin{bmatrix} \mathbf{p}_{s+1}^- \\ \mathbf{p}_{s+1}^+ \end{bmatrix} - \begin{bmatrix} \underline{\mathbf{M}}_s^- & \underline{\mathbf{M}}_s^+ \\ \underline{\mathbf{N}}_s^- & \underline{\mathbf{N}}_s^+ \end{bmatrix} \begin{bmatrix} \underline{\mathbf{E}}_s & \\ & \underline{\mathbf{E}}_s^{-1} \end{bmatrix} \begin{bmatrix} \mathbf{p}_s^- \\ \mathbf{p}_s^+ \end{bmatrix}$$

$$= \underline{\mathbf{D}}_s \exp\left[\underline{\Lambda}(z_s - \eta_s)\right] \underline{\mathbf{D}}_s^{-1} \mathbf{S}^*. \quad \text{(A-8)}$$

At $z = 0$, we have the stress free conditions

$$\underline{\mathbf{N}}_1^- \mathbf{p}_1^- + \underline{\mathbf{N}}_1^+ \mathbf{p}_1^+ = \mathbf{0}, \quad \text{(A-9)}$$

and at $z \to \infty$, we must impose

$$\mathbf{p}_{N+1}^+ = \mathbf{0}. \quad \text{(A-10)}$$

In the global matrix formulation, the local coefficients $\mathbf{p}_m^-$ and $\mathbf{p}_m^+$ are assembled into a global vector that is solved by the Gaussian elimination method with proper scaling and partial pivoting (Chin et al., 1984; Schmidt and Tango, 1986). The global matrix formulation has several important advantages over the Thomson-Haskell propagator matrix technique: (1) any number of sources can be treated conveniently because the fields produced by multiple sources are simply superposed, which is especially important for properly handling the source borehole radiation in the crosswell modeling (Ben-Menahem and Kostek, 1991; Kurkjian et al., 1994; Gibson, 1992); (2) any number of receivers can be treated with only one solution pass since the wavefields are found in all layers simultaneously; and (3) time consuming stability problems do not arise because there is no need for an evaluation of exponential with positive real argument (Peng, 1993).